Journal of Solar Energy Research (JSER)

Journal homepage: www.jser.ut.ac.ir

Artificial Neural Network-Based Maximum Power Point Tracking Control for Power Quality Enhancement in a Single-Phase Grid-Connected Photovoltaic System

Harish Sita[a], Parimalasundar Ezhilvannan[b, *], S. Muthukaruppasamy[c]

[a]*Department of Electrical and Electronics Engineering, Mother Theresa Institute of Engineering and Technology, Chittoor, India*
[b]*Department of Electrical and Electronics Engineering, Saveetha School of Engineering, Saveetha Institute of Medical and Technical Sciences (SIMATS), Chennai, India*
[c]*Department of Electrical and Electronics Engineering, Velammal Institute of Technology, Panjetty, India*

ARTICLE INFO

Article Type:

Research Article

Received:2026.05.13
Accepted in revised form:2026.08.03

Keywords:
Artificial Neural Network; Clean Energy Integration; Grid-Connected Photovoltaic System; Maximum Power Point Tracking; Power Quality

A B S T R A C T

Grid-connected photovoltaic (PV) systems require accurate maximum power point tracking (MPPT), stable direct-current (DC)-link voltage regulation, and improved grid power quality under variable irradiance and temperature. Conventional MPPT methods often exhibit tracking delays and steady-state oscillations and have a limited ability to maintain low harmonic distortion in the grid current under dynamic operating conditions. This simulation-based work develops an artificial neural network (ANN)-based MPPT control strategy for improving power extraction, DC-link stability, and grid-current quality in a single-phase grid-connected PV system. The ANN controller uses irradiance, cell temperature, PV voltage, current, and power as input variables to estimate the voltage reference corresponding to the maximum power point. The error between the predicted reference voltage and the measured PV voltage is used to adjust the duty cycle of the DC–DC boost converter, while the regulated DC-link supports synchronized inverter operation. Under the simulated operating conditions, the system attained a PV voltage of 192 V, a PV current of 0.308 A, and an output power of 59.17 W, a duty cycle of 0.55, a DC-link voltage of 426 V, a switching frequency of 25 kHz, an RMS grid voltage of 230 V, and a grid-current THD of 3.42%.

*Corresponding Author Email: parimalpsg@gmail.com

Cite this article: Sita,H , Ezhilvannan,P and S,M . (2026). Artificial Neural Network-Based Maximum Power Point Tracking Control for Power Quality Enhancement in a Single-Phase Grid-Connected Photovoltaic System. Journal of Solar Energy Research, 11(3), 3967-3981. doi: 10.22059/jser.2026.414342.1740

DOI: 10.22059/jser.2026.414342.1740

1. Introduction

The increasing penetration of photovoltaic (PV) generation into residential, commercial, and utility-scale power networks has intensified the need for efficient energy extraction, stable power conversion, and reliable grid integration. The electrical characteristics of a PV array vary nonlinearly with solar irradiance, cell temperature, partial shading, module ageing, and load conditions. These variations continuously shift the maximum power point (MPP), making maximum power point tracking (MPPT) essential for extracting the available solar energy. In grid-connected PV systems, however, effective power extraction alone is insufficient. MPPT operation must be coordinated with direct-current (DC)-link voltage regulation, converter switching, inverter synchronization, and grid-current control. Inadequate coordination among these stages can result in power loss, slow transient response, operating-point oscillation, DC-link voltage fluctuation, and increased harmonic distortion in the injected grid current.

Conventional MPPT techniques, particularly Perturb and Observe (P&O) and Incremental Conductance (INC), are widely adopted because of their simple structure, low computational burden, and ease of implementation. Nevertheless, fixed-step P&O control generally produces steady-state oscillation around the MPP, while rapid changes in irradiance may cause incorrect tracking decisions. INC offers improved tracking under changing environmental conditions but remains dependent on the selected step size and measurement accuracy. These limitations become more significant when the PV source is connected to a grid through multiple power-conversion stages. Recent developments in grid modernization and energy-storage integration have therefore emphasized the importance of coordinated and sustainable power-management strategies [1]. Artificial neural network (ANN)-based energy management has also been investigated in hybrid microgrids with state-of-charge-supervised storage and multiple grid-operating modes, demonstrating the ability of data-driven controllers to represent nonlinear energy-system behaviour [2]. However, system-level power-management approaches do not necessarily provide direct coordination among PV-side MPPT, boost-converter duty-cycle regulation, DC-link stabilization, and grid-current harmonic control.

Several optimization-based MPPT methods have been introduced to improve tracking performance under nonlinear and time-varying operating conditions. A bio-inspired MFB optimization technique was applied to grid-connected PV systems to enhance maximum-power extraction [3]. Similarly, a neural-network controller combined with ant-colony-optimized proportional–integral control was developed for a PV-based DC microgrid containing battery and supercapacitor storage [4]. Although such approaches can improve operating-point identification, they generally require several tuning parameters and greater computational effort. Other data-driven methods have addressed related PV-system functions. A physics-constrained causal-discovery and graph-neural-network framework was proposed for PV fault diagnosis [5], whereas a seven-level inverter was evaluated for grid-connected operation [6]. These studies improve fault-identification or converter performance; however, they do not jointly evaluate ANN-based MPP prediction, DC-link voltage control, inverter synchronization, and grid-current total harmonic distortion (THD).

ANN-based MPPT has received considerable attention because neural networks can learn nonlinear relationships among irradiance, temperature, PV voltage, PV current, and output power. A flexible ANN-based power-point tracker was developed to improve the dynamic response of a grid-connected PV system [7]. ANN-based MPPT was also implemented using a modified flyback converter for PV systems in active buildings [8]. A grey-wolf-optimized deep adaptive neural MPPT technique was introduced for high-efficiency grid-integrated PV operation [9]. In another application, a Levenberg–Marquardt-trained neural controller was employed with a low-input-current-ripple, high-voltage-gain converter in a fuel-cell energy system [10]. These investigations demonstrate the nonlinear approximation and adaptive prediction capabilities of neural networks. However, the use of deep, optimized, or hybrid neural structures may increase training requirements, parameter dependence, controller complexity, and implementation cost.

Other intelligent-control and converter studies have focused on individual functions within grid-connected renewable-energy systems. A dung-beetle-optimized neuro-synergetic controller was applied to a grid-connected PV system [11], while an asymmetrical fifteen-level inverter was experimentally and numerically evaluated using a mixed-frequency carrier strategy [12]. An adaptive MPPT technique was developed to improve grid-integrated PV performance [13]. Under partial-shading conditions, a global MPPT strategy combining high-order sliding-mode control, artificial-bee-colony optimization, and neural-network prediction was proposed [14]. Hybrid deep-neural learning was also applied to improve energy harvesting under complex partial-shading patterns [15]. Although these methods improve tracking or converter performance, their multistage optimization structures can make controller design, parameter tuning, and real-time implementation more demanding.

Grid-interface research has further highlighted the importance of inverter topology, power-flow regulation, fault tolerance, and low-latency control. A common-ground transformerless single-phase inverter topology was derived using graph theory [16]. An optimized neural-network strategy was employed for electric vehicle (EV) charging power-flow control [17], and an edge-optimized embedded system was developed for low-latency fault detection in electrical grids [18]. Robust ANN-based control was investigated for PV integration during grid faults [19], while an assistive power-balancing method was developed for a cascaded H-bridge inverter in a grid-connected PV application [20]. These studies improve specific functions such as converter topology, fault detection, power balancing, or grid-fault response. However, they do not provide a compact single-phase control structure in which PV-side ANN prediction is directly coordinated with boost-converter regulation, DC-link control, and grid-side power-quality evaluation.

More recent investigations have directly addressed MPPT and power quality in grid-connected PV systems. A comparative assessment of conventional MPPT methods demonstrated their ability to optimize the output of grid-tied PV systems, but it did not include ANN-based MPP reference estimation or coordinated DC-link and inverter control [21]. A hybrid ANN–Grey Wolf Optimization (GWO) MPPT method combined with Model Predictive Control (MPC) was developed for electric-vehicle charging under partial-shading conditions [22]. Although effective under complex operating conditions, the combined optimization and predictive-control structure increases computational and implementation requirements. Optimal power-point tracking was also investigated for distributed grid-connected PV systems [23], but a unified assessment of ANN prediction, duty-cycle response, DC-link stability, synchronization, and grid-current distortion was not presented. An ANN-based current-control method improved the power quality of a grid-tied PV system [24]; however, its primary focus was grid-side current regulation rather than coordinated PV-side ANN-MPPT and boost-converter control.

The environmental and implementation characteristics of power converters are also relevant to sustainable PV integration. A life-cycle assessment of a high-step-up non-isolated direct-current–direct-current (DC–DC) converter examined raw-material extraction, manufacturing, operation, and end-of-life stages, demonstrating that converter selection affects both electrical performance and environmental impact [25]. Earlier control and circuit-level studies have also supported the practical implementation of intelligent controllers. A radial basis function neural-network controller combined with a sliding-surface strategy improved nonlinear tracking in a coupled-tank system [26]. A high-speed complementary metal–oxide–semiconductor (CMOS) fuzzy controller demonstrated the feasibility of compact intelligent-control hardware [27], while programmable rational-powered membership-function circuits enabled flexible and high-resolution fuzzy-control implementation [28]. Although these contributions provide useful foundations for neural and fuzzy control, they do not address coordinated MPPT and grid-power-quality enhancement in a single-phase grid-connected PV system.

The reviewed literature indicates that relatively few studies jointly evaluate PV-side power extraction and grid-side power quality using a compact ANN-based control structure. Most existing methods focus on individual functions, including MPP tracking, partial-shading management, fault diagnosis, converter topology, inverter-current control, or energy-storage management. Limited attention has been given to the direct coordination of ANN-based MPP reference estimation, boost-converter duty-cycle regulation, DC-link voltage control, single-phase inverter synchronization, and grid-current THD evaluation. A unified framework is therefore required to improve transient tracking, reduce steady-state oscillation, regulate the converter output, and maintain grid-current quality without relying on an excessively complex hybrid optimization structure.

The main contribution of this study is the coordinated integration of ANN-based MPPT, boost-converter duty-cycle control, DC-link voltage regulation, inverter synchronization, and grid-current harmonic evaluation within a unified simulation framework. The ANN uses solar irradiance, cell temperature, PV voltage, PV current, and PV power as input variables to estimate the voltage reference corresponding to the MPP. The

difference between the predicted reference voltage and the measured PV voltage is used to adjust the duty cycle of the DC–DC boost converter. This control sequence establishes a closed-loop relationship among ANN prediction, MPP operation, converter voltage gain, and DC-link stabilization.
The principal contribution is the simultaneous quantitative assessment of PV source-side and grid-interface performance. Source-side performance is evaluated using tracking accuracy, response time, steady-state oscillation, duty-cycle response, converter ripple, and DC-link voltage stability. Grid-side performance is assessed using voltage–current synchronization, power factor, and grid-current THD. Under the investigated simulation conditions, the proposed ANN-MPPT controller attains a tracking accuracy of 99.20%, a response time of 0.058 s, a steady-state oscillation level of 0.014, a regulated DC-link voltage of 426 V, and a grid-current THD of 3.42%. Comparative simulation results indicate improved tracking response, reduced oscillation, and better grid-current quality relative to the conventional and intelligent MPPT techniques considered. The contribution therefore extends beyond ANN-based MPP prediction by coordinating the PV source, boost converter, DC link, inverter, and grid interface within a common control and evaluation framework.

2. Proposed Methodology

2.1 Overall System Architecture

The proposed system consists of a PV array, an ANN-based MPPT controller, a DC–DC boost converter, a regulated DC-link, a single-phase voltage-source inverter, and a grid-interface control stage, a single-phase voltage-source inverter, and a grid-interface control stage. The control architecture is designed to coordinate PV-side power extraction with converter regulation and grid-side current injection under variations in solar irradiance and cell temperature. The overall operating sequence includes PV-parameter measurement, ANN-based maximum-power-point reference estimation, boost-converter duty-cycle adjustment, DC-link voltage regulation, inverter synchronization, pulse-width modulation (PWM) generation, and grid-current quality evaluation. Solar irradiance G, cell temperature T_C, PV voltage V_{PV} and PV current I_{PV} are measured continuously. The instantaneous PV power is calculated as $P_{PV} = I_{PV} \times V_{PV}$. These environmental and electrical variables form the input vector of the trained ANN model. The ANN estimates the reference voltage $V_{mpp,ref}$ corresponding to the maximum power point. The predicted reference is then compared with the measured PV voltage to determine the voltage-tracking error. This error is used to update the boost-converter duty cycle so that the operating point of the PV array converges toward the maximum-power region. Figure 1 presents the overall architecture of the proposed ANN-based MPPT and grid-integration framework.

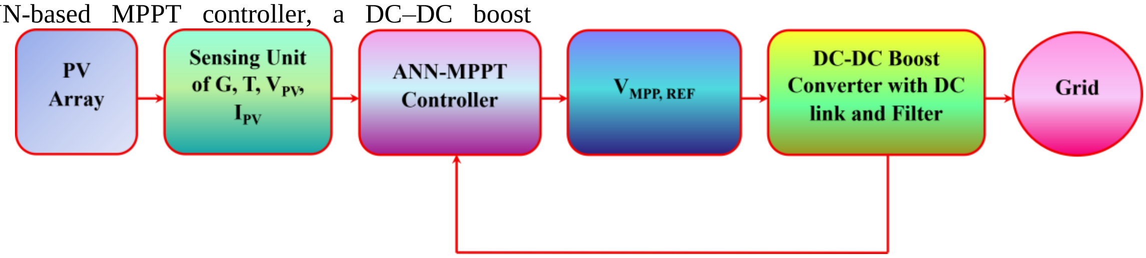

Figure 1. Methodology of the ANN-based MPPT control system showing PV parameter sensing, ANN-based MPP reference estimation, DC–DC boost converter control, DC-link regulation, and grid integration

2.2 ANN-Based Maximum-Power-Point Estimation

The ANN is employed to represent the nonlinear relationship among solar irradiance, cell temperature, PV voltage, PV current, PV power, and the voltage corresponding to the maximum power point. The network contains five input neurons representing G, Tc, V_{PV}, I_{PV}, and P_{PV}. Two hidden layers containing 10 and 8 neurons, respectively, are used to extract the nonlinear features associated with the PV operating condition. A tangent-sigmoid activation function is applied in the hidden layers, while a linear activation function is used at the output layer to estimate $V_{mpp,ref}$. The ANN is trained using the Levenberg–Marquardt back-propagation algorithm, with the mean squared error used as the performance function. A total of 2,500 samples were divided into training, validation, and testing subsets in a ratio of 70:15:15. All input variables are normalized between 0 and 1 before being applied to the network. The normalization procedure prevents variables with larger numerical ranges from dominating the learning process and improves numerical stability during training. The trained model is subsequently incorporated into the closed-loop MPPT controller. At each sampling instant, the measured and calculated PV variables are normalized and applied to the ANN, which generates the required MPP voltage reference.

2.3 Boost-Converter Duty-Cycle Control

The boost converter performs two related functions: it regulates the operating voltage of the PV array and increases the PV-side voltage to the DC-link level required by the inverter. The voltage error is defined as the difference between the ANN-predicted MPP reference voltage and the measured PV voltage. A duty-cycle correction mechanism processes this error and updates the converter reference duty ratio.

When the measured PV voltage differs from $V_{mpp,ref}$, the controller changes the duty cycle to shift the PV operating point toward the predicted maximum-power condition. The duty cycle is restricted to the range of 0.10–0.85 to prevent impractical converter operation and excessive switching stress. A sampling interval of 50 μs is used for ANN evaluation and duty-cycle updating. The resulting duty-cycle reference is compared with a high-frequency carrier signal to generate the PWM gate command for the boost-converter switch. This closed-loop procedure reduces dependence on fixed perturbation steps and limits continuous oscillation around the maximum power point.

2.4 DC-Link Regulation and Grid-Side Control

The output of the boost converter supplies the DC-link capacitor, which acts as the intermediate energy-storage element between the PV source and the inverter. Variations in solar irradiance, PV output power, converter duty cycle, and grid-side power transfer can disturb the DC-link voltage. A proportional–integral (PI) voltage controller is therefore used to regulate the DC-link voltage around its reference value. The difference between the reference and measured DC-link voltages is processed to determine the required active grid-current magnitude.

The single-phase inverter converts the regulated DC-link voltage into alternating current for grid injection. A phase-locked loop (PLL) determines the grid-voltage phase angle and generates a synchronized sinusoidal current reference. The inverter switching signals are produced through PWM so that the injected current follows the reference waveform. The control objective is to maintain the grid current approximately sinusoidal and in phase with the grid voltage, thereby supporting a high-power factor and reducing harmonic distortion.

2.5 Closed-Loop Control Sequence

The complete control procedure is executed repeatedly under changing irradiance and temperature conditions. Initially, the PV and control-system variables are initialized. The controller then measures G, Tc, V_{PV}, I_{PV}, and P_{PV}, forms the ANN input vector, and normalizes the input values. The trained ANN estimates $V_{mpp,ref}$, after which the PV-voltage error and boost-converter duty-cycle reference are calculated. PWM switching commands are generated for the DC–DC converter, and the resulting DC-link voltage is regulated. The grid phase is then identified, inverter switching pulses are generated, and a controlled sinusoidal current is injected into the single-phase grid. Figure 2 illustrates the sequential control process, including PV parameter measurement, ANN-based MPP estimation, duty-cycle updating, DC-link regulation, inverter synchronization, grid-current injection, and power-quality evaluation under variable irradiance and temperature.

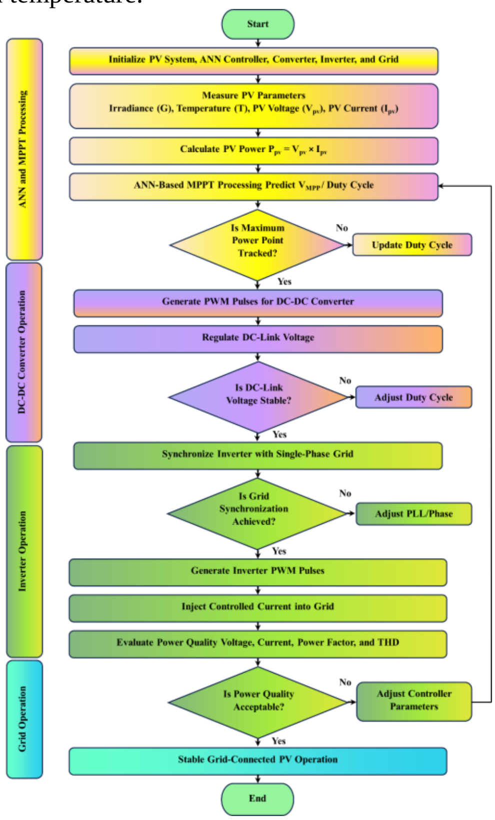

Figure 2. Flowchart of the proposed ANN-based MPPT control algorithm for single-phase grid-connected PV operation under variable irradiance and temperature conditions

Algorithm. ANN-Based MPPT Control Procedure
Step 1: Start the PV-based single-phase grid-connected system.
Step 2: Measure irradiance G and cell temperature Tc.
Step 3: Measure PV voltage V_{pv} and PV current I_{pv}.
Step 4: Calculate PV output power P_{pv}.
Step 5: Form ANN input vector X(k).
Step 6: Normalize the input vector using the training limits.
Step 7: Apply the normalized vector to the trained ANN model.
Step 8: Estimate MPP reference voltage V_{mpp}*.
Step 9: Compare V_{mpp}* with measured PV voltage.
Step 10: Calculate PV voltage error e_v(k).
Step 11: Update boost-converter duty cycle D_{ref}(k).
Step 12: Generate PWM command for the DC-DC converter.
Step 13: Regulate the DC-link voltage.
Step 14: Generate inverter PWM pulses and inject a sinusoidal grid current.
Step 15: Repeat the sequence under changing irradiance and temperature.

3. Mathematical Modelling and Controller Design

The photocurrent generated by the PV module varies with irradiance G and cell temperature T_c, as expressed in Eq. (1) [8, 13, 14, 21].

$$I_{ph} = \left[I_{sc} + K_i (T_c - T_{ref})\right]\frac{G}{G_{ref}} \tag{1}$$

where I_{ph} is the photocurrent, I_{sc} is the short-circuit current, K_i is the temperature coefficient of current, T_c is the cell temperature, T_{ref} is the reference temperature, G is the solar irradiance, and G_{ref} is the reference irradiance. The nonlinear output current of the PV array, including series resistance R_s and shunt resistance R_{sh}, is given in Eq. (2) [8, 13, 14, 21].

$$I_{pv} = I_{ph} - I_o\left[\exp\left(\frac{V_{pv}+I_{pv}R_s}{nV_t}\right)-1\right]-\frac{V_{pv}+I_{pv}R_s}{R_{sh}} \tag{2}$$

where I_{pv} is the PV current, V_{pv} is the PV terminal voltage, I_o is the reverse saturation current, n is the diode ideality factor, V_t is the thermal voltage, R_s is the series resistance, and R_{sh} is the shunt resistance.

The instantaneous power extracted from the PV array is calculated from the measured PV voltage and current, as expressed in Eq. (3) [13, 21, 23]. Table 1 presents the ANN architecture, training parameters, and implementation settings for the grid-connected PV system.

Table 1. ANN-MPPT controller architecture, training parameters, and implementation settings for grid-connected PV operation

ANN Parameters	**Specification**
Network type	Feed-forward back-propagation neural network
Number of input neurons	5
Input variables	G, T_C, V_{PV}, I_{PV}, P_{PV}
Number of hidden layers	2
Neurons in hidden layer 1	10
Neurons in hidden layer 2	8
Number of output neurons	1
Output variable	$V_{mpp,ref}$
Hidden-layer activation function	Tangent sigmoid
Output-layer activation function	Pure linear
Training algorithm	Levenberg-Marquardt back-propagation
Performance function	Mean squared error
Input normalization range	0 to 1
Training–validation–testing ratio	70:15:15
Number of training samples	2500
Maximum training epochs	1000
Target mean squared error	1 x 10^{-6}
Duty-cycle operating limit	0.10 to 0.85
Sampling time	50 µs

$$P_{pv} = V_{pv} I_{pv} \tag{3}$$

where P_{pv} is the PV output power, V_{pv} is the PV voltage, and I_{pv} is the PV current.

At the maximum power point, the derivative of PV power with respect to PV voltage becomes zero, as represented in Eq. (4) [13, 14, 21, 23].

$$\frac{dP_{pv}}{dV_{pv}} = I_{pv} + V_{pv}\frac{dI_{pv}}{dV_{pv}} = 0 \quad (4)$$

where dP_{pv}/dV_{pv} is the PV power slope and dI_{pv}/dV_{pv} is the incremental slope of the PV current-voltage characteristic. The MPP tracking decision can be verified using the incremental conductance condition shown in Eq. (5) [13, 21, 23].

$$\frac{dP_{pv}}{dV_{pv}} = -\frac{I_{pv}}{V_{pv}} \quad (5)$$

where dI_{pv}/dV_{pv} represents incremental conductance and I_{pv}/V_{pv} represents instantaneous conductance. The ANN receives environmental and electrical PV parameters as the input vector, as shown in Eq. (6) [7, 8, 9, 22].

$$X_{ANN}(k) = \left[G(k), T_c(k), V_{pv}(k), I_{pv}(k), P_{pv}(k)\right]^T \quad (6)$$

where $X_{ANN}(k)$ is the ANN input vector at sampling instant k, and the terms $G(k), T_c(k), V_{pv}(k)$, $I_{pv}(k)$, and $P_{pv}(k)$ denote irradiance, temperature, PV voltage, PV current, and PV power, respectively.

The ANN estimates the reference voltage corresponding to the MPP using the nonlinear mapping function represented in Eq. (7) [7, 8, 10, 19, 24].

$$V_{mpp,ref}(k) = f_{ANN}(w, b, X_{ANN}(k)) \quad (7)$$

where $V_{mpp,ref}(k)$ is the predicted MPP reference voltage, f_{ANN} is the ANN mapping function, w denotes the weight matrices, b denotes the bias vectors, and $X_{ANN}(k)$ is the ANN input vector. The ANN-MPPT controller generates the converter duty cycle reference based on the predicted MPP voltage, as expressed in Eq. (8) [4, 7, 8, 22].

$$D_{ref}(k) = D(k-1) + K_D\left[V_{mpp,ref}(k) - V_{pv}(k)\right] \quad (8)$$

where $D_{ref}(k)$ is the reference duty cycle, $D(k-1)$ is the previous duty cycle, K_D is the duty-cycle correction gain, $V_{mpp,ref}(k)$ is the predicted MPP voltage, and $V_{pv}(k)$ is the measured PV voltage. For the ideal DC-DC boost converter, the relationship between the PV input voltage and the DC-link voltage is given in Eq. (9) [8, 10, 22].

$$V_{dc} = \frac{V_{pv}}{1-D} \quad (9)$$

where V_{dc} is the DC-link voltage, V_{pv} is the PV voltage, and D is the duty cycle of the boost converter. The inductor current ripple of the DC-DC converter is obtained from the switching duty ratio, inductance, and switching frequency, as represented in Eq. (10) [8, 10, 22].

$$\Delta I_L = \frac{V_{pv}D}{Lf_s} \quad (10)$$

where ΔI_L is the inductor current ripple, L is the boost-converter inductance, f_s is the switching frequency, V_{pv} is the PV voltage, and D is the duty cycle. The DC-link capacitor voltage ripple under switching operation is estimated using Eq. (11) [4, 10, 22].

$$\Delta V_{dc} = \frac{I_{dc}D}{C_{dc}f_s} \quad (11)$$

where ΔV_{dc} is the DC-link voltage ripple, I_{dc} is the DC-link current, C_{dc} is the DC-link capacitance, D is the duty cycle, and f_s is the switching frequency. The DC-link voltage control error is calculated by comparing the reference voltage with the measured DC-link voltage, as expressed in Eq. (12) [4, 19, 22, 24].

$$e_{dc}(k) = V_{dc,ref}(k) - V_{dc}(k) \quad (12)$$

where $e_{dc}(k)$ is the DC-link voltage error, $V_{dc,ref}(k)$ is the reference DC-link voltage, and $V_{dc}(k)$ is the measured DC-link voltage. The PI voltage controller produces the active grid-current reference using Eq. (13) [4, 19, 22, 24].

$$I_{g,ref}(k) = K_p e_{dc}(k) + K_i \sum_{j=0}^{k} e_{dc}(j) T_s \quad (13)$$

where $I_{g,ref}(k)$ is the grid current reference magnitude, K_p is the proportional gain, K_i is the integral gain, $e_{dc}(j)$ is the DC-link voltage error, and T_s is the sampling time. The inverter injects a sinusoidal current synchronized with the single-phase grid voltage, as represented in Eq. (14) [16, 19, 20, 24].

$$I_{g,ref}(k) = I_{g,ref}\sin(\theta_g) \tag{14}$$

where $I_{g,ref}(k)$ is the instantaneous grid current reference, $I_{g,ref}$ is the peak grid current reference, and θ_g is the grid phase angle obtained from PLL synchronization. The quality of the injected grid current is evaluated using the THD expression given in Eq. (15) [6, 16, 20, 24].

$$THD_i = \frac{\sqrt{\sum_{h=2}^{N} I_h^{\,2}}}{I_1} \times 100\% \tag{15}$$

where THD_i is the current total harmonic distortion, I_h is the RMS value of the h^{th} harmonic current component, I_1 is the RMS value of the fundamental current component, and N is the maximum harmonic order considered.

4. Results and Discussion

4.1 ANN Training Performance

The ANN was trained to estimate the reference voltage corresponding to the maximum power point from five input variables: solar irradiance, cell temperature, PV voltage, PV current, and PV power. The network employed two hidden layers containing 10 and 8 neurons, respectively, with tangent-sigmoid activation functions, while a linear activation function was used in the output layer. The available dataset contained 2500 samples and was divided into training, validation, and testing subsets in a ratio of 70:15:15. The input variables were normalized to the range of 0–1, and the network was trained using the Levenberg–Marquardt back-propagation algorithm with mean squared error as the performance criterion.

Figure 3 presents the variation in mean squared error over the training epochs. The error decreases rapidly during the initial epochs and subsequently approaches a stable minimum, indicating that the network converges without persistent oscillation in the learning process. The similarity among the training, validation, and testing curves suggests that the model maintains comparable prediction behaviour across the three data subsets. Nevertheless, the generalization capability should ultimately be confirmed using operating conditions that are independent of the training dataset.

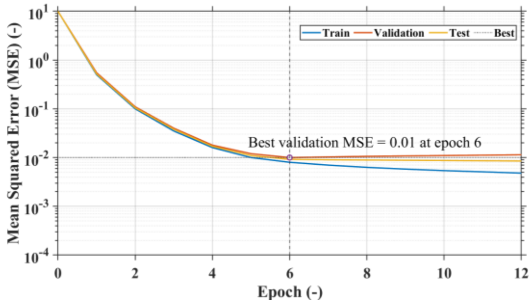

Figure 3. ANN training performance curve showing the variation in mean squared error over the training epochs for evaluating convergence of the ANN-MPPT model

The distribution of prediction errors shown in Figure 4 is concentrated near zero. This distribution indicates that most ANN outputs remain close to their corresponding target values. A narrow error distribution is particularly important for the proposed controller because large reference-voltage prediction errors could produce unnecessary duty-cycle variations and increase oscillation around the maximum power point. The obtained training behaviour therefore supports the use of the ANN as the reference-estimation component of the closed-loop MPPT controller.

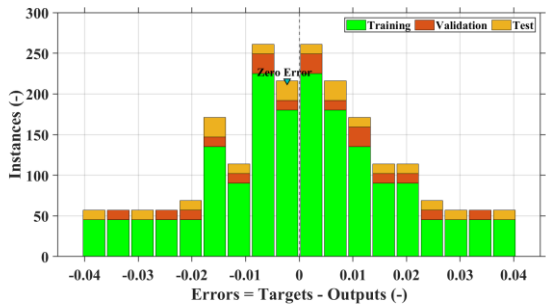

Figure 4. Error histogram of the ANN model for training, validation, and testing data showing the distribution of prediction errors around zero-error region

However, the training curves and error histogram alone do not establish robustness under previously unseen partial-shading patterns, sensor noise, parameter ageing, or grid disturbances.

4.2 MPPT Dynamic Response

The dynamic response of the ANN-based MPPT controller was evaluated by varying solar irradiance from 650 to 1060 W/m² and cell temperature from 25.0 to 29.7°C. The environmental profile presented in Figure 5 shifts the PV operating point and provides a time-varying test condition for evaluating reference estimation, duty-cycle adjustment, and maximum-power-point convergence. The controller continuously measures the environmental and electrical variables, estimates the required maximum-power-point voltage, and adjusts the converter duty cycle according to the difference between the estimated and measured PV voltages.

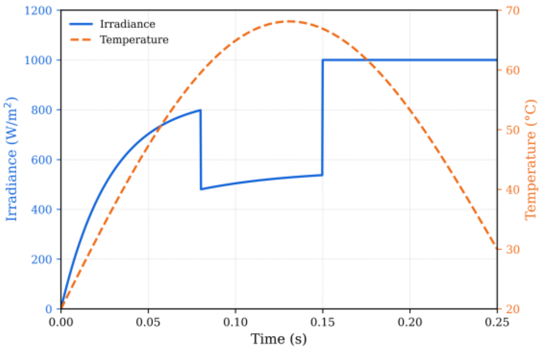

Figure 5. Irradiance and temperature profiles used to evaluate the dynamic tracking performance of the ANN-MPPT controller

Figure 6 shows that the duty cycle changes during the initial transient and settles near 0.55 under the nominal operating condition. This response indicates that the controller modifies the boost-converter operating state to move the PV array toward the predicted maximum-power region.

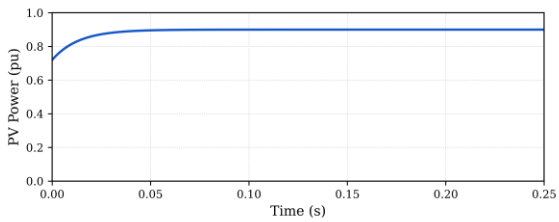

Figure 6. Duty-cycle response of the ANN-MPPT controller showing converter duty-cycle adjustment during maximum power point tracking of the PV system

The corresponding current–voltage and power–voltage characteristics in Figure 7 identify the nonlinear PV operating region and the location of the maximum power point. The PV array configuration and voltage-scaling relationship were selected to produce the reported operating voltage of approximately 192 V, consistent with the current–voltage characteristic shown in Figure 7.

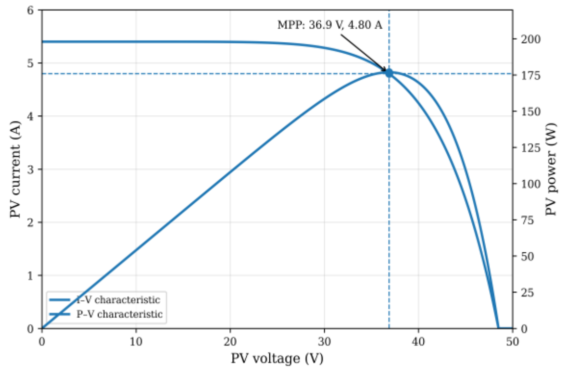

Figure 7. PV current–voltage and power–voltage characteristics under standard test conditions showing the maximum power point operating region

Table 2 summarizes the dynamic MPPT performance at different irradiance and temperature levels. As irradiance increases from 650 to 1060 W/m², the reported tracking time decreases from 0.082 to 0.055 s, while the tracking accuracy increases from 97.40% to 99.35%. Over the same operating range, the reported ripple index decreases from 0.021 to 0.013. At 1000 W/m² and 28.6°C, the controller achieves a tracking accuracy of 99.20%, a response time of 0.058 s, and a ripple index of 0.014. These results indicate improved convergence and reduced steady-state variation at higher irradiance levels under the investigated simulation conditions.

The ripple values reported in Table 2 represent the normalized steady-state power oscillation around the maximum power point.

Table 2. Dynamic MPPT tracking performance of the ANN controller under different irradiance and temperature conditions

Irradiance (W/m²)	**Temperature (°C)**	**Tracking Time (s)**	**Ripple**	**Accuracy (%)**
650	25.0	0.082	0.021	97.40
780	26.2	0.071	0.018	98.10
900	27.4	0.063	0.016	98.80
1000	28.6	0.058	0.014	99.20
1060	29.7	0.055	0.013	99.35

4.3 Converter and DC-Link Performance

The DC–DC boost converter regulates the PV operating voltage and raises it to the level required by the single-phase inverter. The converter duty cycle is generated from the ANN-predicted maximum-power-point voltage and the measured PV voltage. Figure 8 presents the PWM gate signals used to control the boost converter and inverter switches. The switching frequency is maintained at 25 kHz, which represents a compromise among switching losses, converter ripple, and control-response requirements.

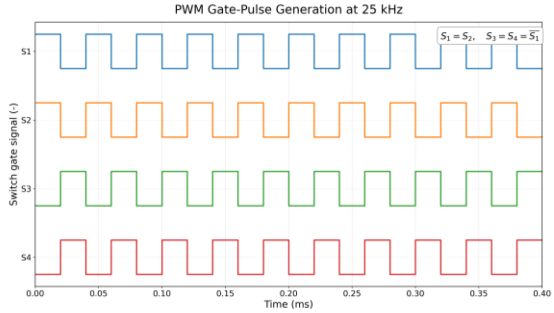

Figure 8. PWM gate-pulse generation for the DC–DC boost converter and single-phase inverter used for controlled power conversion and grid injection

The influence of duty-cycle variation on the converter and DC-link performance is summarized in Table 3. When the duty cycle increases from 0.50 to 0.60, the PV voltage increases from 184 to 200 V and the DC-link voltage rises from 368 to 500 V. The corresponding PV output power increases from 52.40 to 63.70 W, whereas the reported ripple decreases from 1.42 to 0.92. At the selected nominal operating point, a duty cycle of 0.55 produces a PV voltage of 192 V, a PV output power of 59.17 W, and a DC-link voltage of approximately 426 V. These values demonstrate the direct influence of duty-cycle regulation on converter voltage gain, PV power extraction, and DC-link operating conditions.

Table 3. Effect of duty-cycle variation on PV voltage, DC-link voltage, PV output power, and converter ripple

Duty Cycle	PV Voltage (V)	DC-Link Voltage (V)	PV Power (W)	Ripple
0.50	184	368	52.40	1.42
0.53	188	400	55.80	1.21
0.55	192	426	59.17	1.04
0.58	196	467	61.30	0.98
0.60	200	500	63.70	0.92

Figure 9 shows the transient response of the DC-link voltage. The voltage increases from its initial value and progressively approaches the 426 V reference with diminishing oscillation. After the transient interval, the DC-link voltage remains close to the reference level, indicating that the combined boost-converter and voltage-control stages can maintain the inverter input voltage under the simulated conditions.

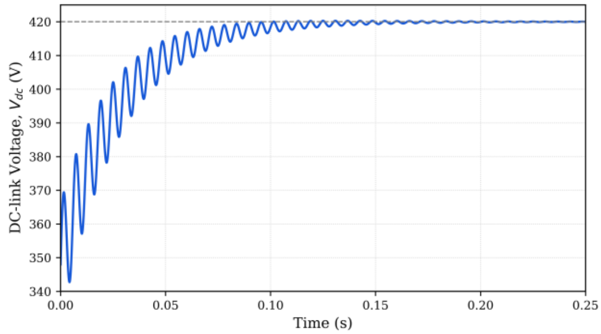

Figure 9. DC-link voltage regulation response showing the ability of the boost converter and ANN-based MPPT controller to maintain a stable DC-link voltage

4.4 Grid-Side Power Quality

The regulated DC-link voltage supplies the single-phase inverter, which converts the available DC power into alternating current for grid injection. The inverter-current reference is synchronized with the grid voltage using the estimated grid phase angle. Pulse-width modulation is then applied to generate the switching signals required to ensure that the injected current follows the sinusoidal reference. The primary grid-side objectives are to maintain voltage–current synchronization, achieve a high-power factor, and limit the harmonic content of the injected current.

Figure 10 presents the grid-voltage and grid-current waveforms. The close phase alignment between the grid-current and grid-voltage waveforms indicates predominantly active-power transfer and synchronized inverter operation. At the nominal operating point, the grid voltage is approximately 230 V RMS, the frequency is 50 Hz, and the power factor is reported as 0.992.

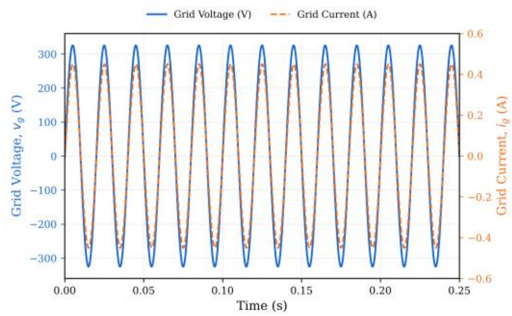

Figure 10. Grid voltage and grid current waveforms showing synchronization between the inverter output current and the single-phase grid voltage

The harmonic spectrum shown in Figure 11 indicates a dominant fundamental current component and smaller higher-order harmonic components. The calculated grid-current THD at the nominal operating point is 3.42%. Table 4 shows that, as the grid voltage increases from 228 to 232 V, the grid current rises from 0.238 to 0.268 A.

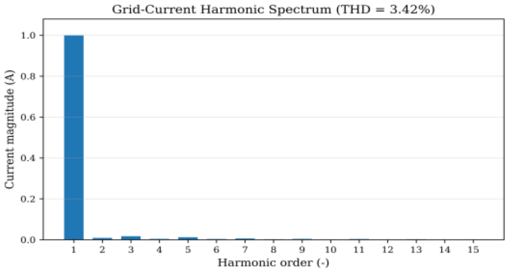

Figure 11. Harmonic spectrum of the injected grid current showing the total harmonic distortion of the grid current under ANN-based MPPT operation

Table 4. Grid-side power-quality performance showing voltage, current, frequency, THD, and power factor under ANN-MPPT operation

Grid Voltage (V)	Grid Current (A)	Frequency (Hz)	THD (%)	Power Factor
228	0.238	49.96	3.91	0.982
229	0.246	49.98	3.66	0.987
230	0.257	50.00	3.42	0.992
231	0.262	50.01	3.38	0.993
232	0.268	50.02	3.35	0.994

Over the same range, the reported power factor improves from 0.982 to 0.994, while current THD decreases from 3.91% to 3.35%. The frequency remains close to 50 Hz, varying between 49.96 and 50.02 Hz.

These results indicate that the inverter controller maintains synchronized current injection and relatively low harmonic distortion under the tested grid-voltage range. The reported harmonic performance applies to the investigated simulation conditions and does not constitute a complete compliance assessment against the requirements of IEEE 519 or IEEE 1547. Although the obtained grid-current THD is relatively low, complete grid-code compliance requires additional assessment of voltage level, harmonic-order limits, point-of-common-coupling conditions, and measurement procedures.

4.5 Comparative Assessment

The performance of the ANN-based MPPT controller was compared with that of the P&O, INC, fuzzy-logic MPPT, and adaptive MPPT methods. Table 5 reports that the ANN-MPPT method achieves a tracking accuracy of 99.20%, a response time of 0.058 s, a steady-state oscillation level of 0.014, and a grid-current THD of 3.42%. Under the reported comparison conditions, P&O achieves 92.40% accuracy, a response time of 0.118 s, an oscillation level of 0.072, and a THD of 4.82%. INC achieves 95.10% accuracy, a response time of 0.095 s, an oscillation level of 0.051, and a THD of 4.31%. The fuzzy-logic and adaptive MPPT methods show intermediate performance.

Table 5. Comparative MPPT performance of conventional and intelligent techniques in terms of accuracy, response time, oscillation level, and THD

Method	Accuracy (%)	Response Time (s)	Oscillation Level	THD (%)
P&O MPPT	92.40	0.118	0.072	4.82
Incremental Conductance MPPT	95.10	0.095	0.051	4.31
ANN-MPPT	99.20	0.058	0.014	3.42
Fuzzy Logic MPPT	98.60	0.064	0.019	3.55
Adaptive MPPT	97.90	0.071	0.023	3.74

Figure 12 compares the methods in terms of tracking accuracy, response time, DC-link ripple, PV output power, steady-state error, and THD reduction.

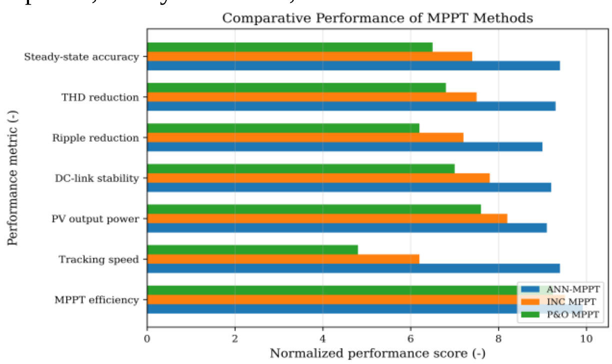

Figure 12. Comparative performance analysis of different MPPT techniques based on tracking accuracy, response time, DC-link ripple, PV output power, steady-state error, and THD reduction

Figure 13 presents a normalized radar-chart comparison based on tracking accuracy, dynamic response, DC-link stability, ripple reduction, synchronization, THD reduction, and overall power-quality improvement. Both figures indicate that the ANN-MPPT controller provides the highest combined performance among the evaluated methods under the investigated simulation conditions, particularly in tracking speed, steady-state stability, and current-harmonic reduction.

The comparative results should be interpreted cautiously. A valid comparison among the methods requires identical PV ratings, irradiance profiles, sampling intervals, converter parameters, switching frequencies, controller limits, and performance definitions.

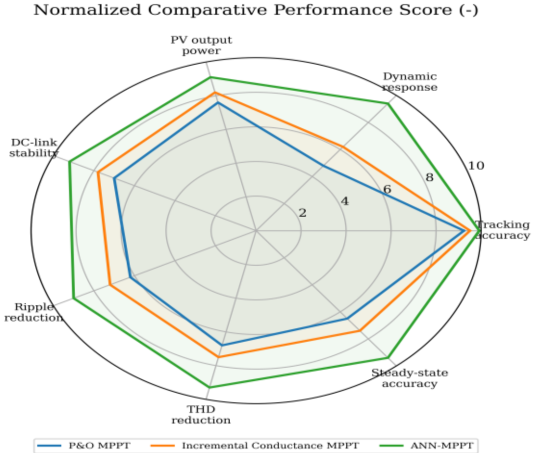

Figure 13. Radar chart comparison of P&O MPPT, INC MPPT, and ANN-MPPT based on tracking accuracy, dynamic response, DC-link stability, ripple reduction, synchronization, and THD reduction

Table 6 presents the proposed scenarios for future validation under partial shading and grid disturbances. Experimental implementation, real-time processor testing, computational-cost assessment, sensor-noise analysis, and validation under global maximum-power-point conditions are necessary before conclusions about practical superiority can be established. Table 7 further compares the proposed method with recent MPPT and grid-current-control approaches. The proposed framework provides coordinated ANN-based MPP estimation, boost-converter duty-cycle control, DC-link regulation, grid synchronization, and THD evaluation.

Table 6. Extended validation scenarios for evaluating ANN-MPPT robustness under partial shading and grid disturbances

Test Case	**Operating Condition**	**Purpose**	**Parameters to Report**
Uniform irradiance	650-1060 W/m²	Base MPPT tracking validation	Tracking time, PV power, duty cycle, THD
Partial shading case 1	1000-800-600 W/m²	Global maximum power point (GMPP) tracking under multiple peaks	GMPP power, tracking time, DC-link ripple
Partial shading case 2	1000–700-400 W/m²	Severe shading validation	GMPP accuracy, steady-state oscillation
Voltage sag	A grid voltage of 0.8 per unit (p.u.) for a short duration	Grid fault response	DC-link overshoot, settling time, grid current THD
Frequency deviation	49-51 Hz	Synchronization robustness	PLL response, grid current phase, power factor
Distorted grid voltage	Harmonic distortion in grid voltage	Power-quality validation	Grid-current THD, waveform distortion

Table 7. Comparative assessment of the proposed ANN-MPPT method with recent MPPT and power-quality control methods

Method	**Main focus**	**Reported performance**	**Limitation relative to the present work**
Proposed ANN-MPPT	MPPT, DC-link regulation, grid THD	99.20% accuracy, 0.058 s response, 3.42% THD	Simulation-level validation only

INC MPPT [21]	Grid-tied PV MPPT	98.7% efficiency for I&C	Conventional MPPT; no ANN-based prediction
ANN–GWO–MPC [22]	Partial shading and EV charging	THD reduced to 1.56%	More complex hybrid control
Radial Basis Function Neural Network–Ant Colony Optimization (RBFNN–ACO) [23]	Distributed grid PV MPPT	Tracking error within 2.5%	Limited grid-current THD discussion
ANN current control [24]	Grid-tied inverter current control	dSPACE-based validation	Focuses on inverter-current control rather than ANN-based MPPT

5. Conclusion

This study presented an ANN-based MPPT controller for a single-phase grid-connected photovoltaic system. The proposed framework coordinated maximum-power-point estimation, boost-converter duty-cycle control, DC-link voltage regulation, inverter synchronization, and grid-current quality assessment. Under the investigated simulation conditions, the controller achieved 99.20% tracking accuracy, a response time of 0.058 s, a steady-state oscillation level of 0.014, a regulated DC-link voltage of approximately 426 V, and a grid-current THD of 3.42%. The results indicate that the ANN-based approach provides faster tracking, reduced operating-point oscillation, improved DC-link stability, and better grid-current quality than that achieved by the conventional MPPT methods considered. However, the present findings are limited to simulation-based validation. Future work should evaluate the controller under partial shading, rapid irradiance transitions, grid-voltage sag, frequency deviation, distorted grid voltage, sensor noise, and PV-module ageing. Hardware-in-the-loop testing and experimental validation using a real-time processor should also be conducted. Further investigations may include adaptive online ANN training, reduced computational complexity, converter-efficiency analysis, thermal and switching-loss evaluation, and integration with battery-energy-storage systems to improve practical reliability and grid-support capability.

Nomenclature

AC	Alternating current
ANN	Artificial neural network
b	Bias vector of ANN model
C_{dc}	DC-link capacitance (F)
D	Boost converter duty cycle
$D_{ref}(k)$	Reference duty cycle at sampling instant k
DC	Direct current
$DC–DC$	Direct-current-to-direct-current converter
dI_{PV}/dV_{PV}	Incremental slope of PV current-voltage characteristic (A/V)
dP_{PV}/dV_{PV}	PV power slope with respect to PV voltage (W/V)
$e_{dc}(k)$	DC-link voltage error at sampling instant k (V)
$e_v(k)$	PV voltage error at sampling instant k (V)
f_s	Switching frequency (Hz)
G	Solar irradiance (W/m²)
G_{ref}	Reference solar irradiance (W/m²)
I_1	RMS value of fundamental current component (A)
I_{dc}	DC-link current (A)
$I_{g,ref}(k)$	Grid current reference at sampling instant k (A)
I_h	RMS value of the h^{th} harmonic current component (A)
I_o	Reverse saturation current of PV diode (A)
I_{Ph}	Photocurrent generated by PV module (A)
I_{PV}	PV output current (A)
I_{SC}	Short-circuit current (A)
K_D	Duty-cycle correction gain
K_i	Temperature coefficient of current (A/°C)
$K_{i,pi}$	Integral gain of PI controller
K_P	Proportional gain of PI controller
L	Boost converter inductance (H)

MPP	Maximum power point
MPPT	Maximum power point tracking
N	Maximum harmonic order considered for THD calculation
n	Diode ideality factor
P&O	Perturb-and-observe method
PI	Proportional-integral controller
P_{PV}	PV output power (W)
PV	Photovoltaic
PWM	Pulse-width modulation
RMS	Root mean square
R_S	Series resistance of PV model (Ω)
R_{sh}	Shunt resistance of PV model (Ω)
T_C	Cell temperature (°C)
T_{ref}	Reference temperature (°C)
THD	Total harmonic distortion (%)
THD_i	Current total harmonic distortion (%)
T_S	Sampling time (s)
V_{dc}	DC-link voltage (V)
$V_{dc,ref}(k)$	Reference DC-link voltage at sampling instant *k* (V)
V_g	Grid output voltage (V)
$V_{mpp,ref}(k)$	Predicted MPP reference voltage at sampling instant *k* (V)
V_{PV}	PV terminal voltage (V)
V_t	Thermal voltage (V)
w	Weight matrix of ANN model
$X_{ANN}(k)$	ANN input vector at sampling instant *k*
ΔI_L	Inductor current ripple (A)
ΔV_{dc}	DC-link capacitor voltage ripple (V)
θ_g	Grid phase angle obtained from PLL synchronization (rad)

References

[1] Arun, M., Samal, S., Barik, D., Chandran, S. S. R., Tudu, K., & Praveenkumar, S. (2025). Integration of energy storage systems and grid modernization for reliable urban power management toward future energy sustainability. *Journal of Energy Storage*, *131*, 115830. DOI: 10.1016/j.est.2025.115830

[2] Badoruzzaman, Md., Shuvo, J. I., Islam Anik, S. T., Ahmad, S., Huda, A. S. N., Ahmed, T., & Karimi, M. (2025). Artificial neural network-based power management for hybrid microgrid with SoC-supervised storage and dual-mode grid operation. *Energy Conversion and Management: X*, *28*, 101316. DOI: 10.1016/j.ecmx.2025.101316

[3] Ballouti, A., Chouiekh, M., Latrach, H., Abad, A., Ameziane, H., Zakriti, A., El Mourabit, Y., Meshref, H., Masud, M., Karmouni, H., & Abouhawwash, M. (2026). Enhancing grid connected photovoltaic systems performance using a bio-inspired MFB algorithm for efficient maximum power point tracking. *Energy Reports*, *15*, 109210. DOI: 10.1016/j.egyr.2026.109210

[4] Benfatma, H., Khouidmi, H., & Bessedik, B. (2025). Neural network and ACO algorithm-tuned PI controller for MPPT in a hybrid battery-supercapacitor energy storage system within DC micro-grid photovoltaic installations. *Journal of Energy Storage*, *120*, 116499. DOI: 10.1016/j.est.2025.116499

[5] Du, T., Li, Q., Ren, J., Peng, B., & Li, B. (2025). Photovoltaic system fault diagnosis method based on physics-Constrained causal discovery and causal perception graph neural network. *Energy*, *340*, 139248. Doi: 10.1016/j.energy.2025.139248

[6] E, P., S, J., T, D., & V S, C. (2023). Performance analysis of a seven-level multilevel inverter in grid-connected systems. *International Journal of Electrical and Electronics Engineering*, *10*(6), 9–22. DOI: 10.14445/23488379/IJEEE-V10I6P102

[7] Guerrero-Rodríguez, N. F., Mercado-Ravelo, R., Batista-Jorge, R. O., Núñez-Ramírez, V., Ramírez-Rivera, Francisco. A., Ramos Ciprian, R. D., Rey-Boué, A. B., & Reyes-Archundia, E. (2025). Artificial neural network-based flexible power point tracking for enhanced dynamic response of grid-connected photovoltaic systems. *Energy Reports*, *14*, 3495–3513. DOI: 10.1016/j.egyr.2025.10.018

[8] Gul, S., Malik, S. M., Sun, Y., & Alsaif, F. (2024). An artificial neural network based mppt control of modified flyback converter for pv systems in active buildings. *Energy Reports*, *12*, 2865–2872. DOI: 10.1016/j.egyr.2024.08.082

[9] Mary A, A. M., & K, R. K. (2025). Grey wolf optimized deep adaptive neural MPPT technique for high-efficiency grid integrated photovoltaic systems. *Energy*, *341*, 139501. DOI: 10.1016/j.energy.2025.139501

[10] Özden, M., Ertekin, D., & Siano, P. (2025). Levenberg-marquardt algorithm-based neural network smart control strategy for a low-input current ripple and high-voltage gain power converter in fuel-cells energy systems. *IEEE Access*, *13*, 3613–3631. DOI: 10.1109/ACCESS.2024.3524378

[11] Palanichamy, P., Rajaram, G., Krishnasamy, R., Giri, J., Kanan, M., Sundararaman, S., R, P. T., & S, G. (2025). A distinctive dung beetle optimized (Dbo) – neuro synergetic aquila controller (Nsac) for grid-pv systems. *Results in Engineering*, *25*, 104239. DOI: 10.1016/j.rineng.2025.104239

[12] Paramasivan, M., Prasad, T. N., & Vanchinathan, K. (2025). Experimental and numerical investigations on amalgamation of mixed frequency carrier based asymmetrical 15 level multilevel inverter. *Electrical Engineering*, *107*(5), 5861–5875. DOI: 10.1007/s00202-024-02854-2

[13] Prajapati, S., Garg, R., & Mahajan, P. (2024). Novel adaptive MPPT technique for enhanced performance of grid integrated solar photovoltaic system.

Computers and Electrical Engineering, *120*, 109648. DOI: 10.1016/j.compeleceng.2024.109648

[14] Rizki, H., Lamzouri, F. E., Boufounas, E.-M., Amrani, A. E., & Bejjit, L. (2025). Advanced global MPPT strategy for PV systems using high-order sliding mode control, ABC optimization, and neural network prediction under partial shading conditions. *Computers and Electrical Engineering*, *127*, 110562. DOI: 10.1016/j.compeleceng.2025.110562

[15] SeyedShenava, S., Zare, P., & Davoudkhani, I. F. (2025). Maximizing solar energy harvesting efficiency: Optimal hybrid deep neural learning -based MPPT for Photovoltaic systems under complex partial shading conditions. *Sustainable Computing: Informatics and Systems*, *47*, 101159. DOI: 10.1016/j.suscom.2025.101159

[16] Yao, Z., & Xu, Q. (2025). Topology derivation method of common-ground transformerless single-phase inverters based on graph theory. *IEEE Transactions on Power Electronics*, *40*(3), 4510–4521. DOI: 10.1109/TPEL.2024.3503515

[17] Singh, A. P., Kumar, Y., & Sawle, Y. (2026). Electric vehicle charging system power flow control using artificial gorilla troops optimized neural network. *Journal of Energy Storage*, *152*, 120742. DOI: 10.1016/j.est.2026.120742

[18] Tankala, D. K., A, R. K., S, N. R., P, J., & Muniyandy, E. (2025). Edge-optimized embedded system for low-latency fault detection in electrical grids. *International Journal of Electrical and Electronics Engineering*, *12*(11), 207–218. DOI: 10.14445/23488379/IJEEE-V12I11P117

[19] Tebaa, M., & Ouassaid, M. (2026). Robust artificial neural network-based control for photovoltaic integration under grid fault conditions. *Results in Engineering*, *29*, 109473. DOI: 10.1016/j.rineng.2026.109473

[20] Tanguturi, J., & Keerthipati, S. (2025). Assistive grid power scheme to enhance power balancing capacity of solar photovoltaic chb inverter for grid-connected application. *IEEE Transactions on Industrial Electronics*, *72*(9), 9207–9216. DOI: 10.1109/TIE.2025.3544210

[21] Elsafi, A., Almohammedi, A. A., Balfaqih, M., Balfagih, Z., & Sabri, S. (2025). Comparative analysis of maximum power point tracking methods for power optimization in grid tied photovoltaic solar systems. *Discover Applied Sciences*, *7*, 976. DOI: 10.1007/s42452-025-07606-w

[22] Hakam, Y., Ahessab, H., Tabaa, M., ELHadadi, B., & Gaga, A. (2025). Hybrid ANN–GWO MPPT with MPC-based inverter control for efficient EV charging under partial shading conditions. *Science Progress*, *108*(2), 00368504251331835. https://doi.org/10.1177/00368504251331835

[23] Yang, P., Weng, H., & Zhong, Y. (2026). Application of optimal power point tracking technology in distributed grid-connected photovoltaic systems. *PLOS ONE, 21*(4), e0344494. DOI: 10.1371/journal.pone.0344494

[24] Abu-Zaher, M., Shen, K., Aly, M., Houran, M. A., Sayed, K., Abo-Khalil, A. G., & Hassan, A. (2025). Power quality enhancement in grid-tied photovoltaic systems through artificial neural network-based current control strategies. *International Journal of Electrical Power & Energy Systems, 172*, 111362. DOI: 10.1016/j.ijepes.2025.111362

[25] Teymoriyan, M., Naderi Saatlo, A. and Salimi, M. (2024). Environmental Aspect of Using a High Step-Up No Isolated DC-DC Converter for Solar Photovoltaic Applications: Life Cycle Assessment Point of View. *Journal of Solar Energy Research*, *9(3)*, 1942-1953. DOI: 10.22059/jser.2024.375177.1405

[26] Aliasghary, M., Naderi, A., Ghasemzadeh, H., & Pourazar, A. (2011). Design of radial basis function neural networks controller based on sliding surface for a coupled tanks system. In *2011 6th IEEE Joint International Information Technology and Artificial Intelligence Conference* (pp. 8–12). IEEE. DOI: 10.1109/ITAIC.2011.6030138

[27] Naderi, A., Aliasghary, M., Pourazar, A., & Ghasemzadeh, H. (2011). A 19 MFLIPS CMOS fuzzy controller to control continuously variable transmission ratio. In *2011 7th Conference on Ph.D. Research in Microelectronics and Electronics* (pp. 45–48). IEEE. DOI: 10.1109/PRIME.2011.5966213

[28] Naderi, A., Mojarrad, H., Ghasemzadeh, H., Khoei, A., & Hadidi, K. (2009). Circuit implementation of programmable high-resolution rational-powered membership functions in standard CMOS technology. In *IEEE EUROCON 2009* (pp. 1236–1241). IEEE. DOI: 10.1109/EURCON.2009.5167794